

We are IntechOpen, the world's leading publisher of Open Access books Built by scientists, for scientists

6,900

Open access books available

186,000

International authors and editors

200M

Downloads

Our authors are among the

154

Countries delivered to

TOP 1%

most cited scientists

12.2%

Contributors from top 500 universities



WEB OF SCIENCE™

Selection of our books indexed in the Book Citation Index
in Web of Science™ Core Collection (BKCI)

Interested in publishing with us?
Contact book.department@intechopen.com

Numbers displayed above are based on latest data collected.
For more information visit www.intechopen.com



Creation and Evaluation of Atomically Ordered Side- and Facet-Surface Structures of Three-Dimensional Silicon Nano-Architectures

Azusa N. Hattori and Ken Hattori

Abstract

The realization of three-dimensional (3D)-architected nanostructures, that is, the transformation from novel two-dimensional (2D) film-based devices to 3D complex nanodevices, is of crucial importance with the progress of scaling down devices to nanometer order. However, little attention has been devoted to controlling the atomic ordering and structures of side-surfaces on 3D structures, while techniques for controlling and investigating 2D surfaces, namely, surface science, have been established only for planar 2D surfaces. We have established an original methodology that enables atomic orderings and arrangements of surfaces with arbitrary directions to be observed on 3D figured structures by developing diffraction and microscopy techniques. An original technique, namely, directly and quantitatively viewing the side- and facet-surfaces at the atomic scale by reflection high-energy electron diffraction (RHEED) and low-energy electron diffraction (LEED), can be used to determine process parameters in etching. This chapter introduces methods of evaluation by RHEED and LEED based on a reciprocal space map and methods of creating various atomically flat {111} and {100} side-surfaces of 3D Si nano-architectures and tilted {111} facet-surfaces fabricated by lithography dry and wet etching processes, followed by annealing treatment in vacuum.

Keywords: side-surface, facet-surface, atomically flat, Si, lithography, dry etching, wet etching, electron diffraction, reciprocal space map

1. Introduction

The significance of nanostructuring techniques has increased with the progress of scaling down devices to nanometer order in accordance with Moore's law [1]. The realization of three-dimensional (3D)-architected nanostructures, that is, the transformation from novel two-dimensional (2D) film-based planar devices to 3D complex and multifunctional nanodevices, is of crucial importance to future electronic applications [2, 3], the so-called More Moore. So far, various nanofabrication techniques have been proposed and developed with different levels of success. In many cases, materials grown on substrates are affected by substrate structural characteristics such as shape, roughness, and dimensionality. Three-dimensional patterned substrates

prepared by a conventional lithographic method can be used to form 3D nanostructures. Although considerable attention has been devoted to controlling the size, shape, and positioning in research on 3D patterning, little attention has been focused on the atomic ordering of arbitrarily oriented surfaces on 3D patterned substrates. The realization of perfect surfaces on 3D structures is required to produce high-quality samples. Since material growth starts on a surface, the surface condition clearly determines the structural and physical properties of the grown material.

Although techniques for studying 2D surfaces, namely, surface science, have been intensively developed and established, little attention has been devoted to controlling the atomic ordering and structures of side-surfaces on 3D architectures. Fabrication techniques for 3D nanoscale structures that are promising for 3D integrated circuits have been individually developed from surface science.

The subject of study should be changed from 2D planar surfaces to 3D assembly surfaces to enable atomically ordered nanofabrication on vertical side-surfaces and/or tilted facet-surfaces in 3D space (**Figure 1**). For this purpose, a simple and accurate structure evaluation technique is required. Currently, scanning electron microscopy (SEM) is widely used for the observation of 3D nanostructures. However, SEM cannot be used to evaluate structures involving atomic ordering. On the other hand, transmission electron microscopy (TEM) is a powerful technique for examining the atomic structure of 3D nanomaterials, but it is destructive and not convenient. An alternative technique is a diffraction method. Reflection high-energy electron diffraction (RHEED) enables the examination of surface properties such as atomic ordering, surface roughness (flatness), and surface homogeneity [4]. Low-energy electron diffraction (LEED) is also a conventional and nondestructive surface observation technique [5]. To apply these techniques to 3D structured samples with various oriented surfaces, instead of 2D planar samples, an appropriate alignment of the incident electron beam considering the configuration in 3D space is indispensable [6–9].

In this chapter, we first show how to obtain and evaluate RHEED and LEED patterns from 3D structured samples by explaining the principle of diffraction. Then, we demonstrate creating and evaluating atomically ordered side- and facet-surface structures of 3D silicon nano-architectures. Finally, we discuss novel structures that have been constructed on 3D patterned Si to form 3D interconnected structures and their physical properties.

2. Theory (methodology)

2.1 Reciprocal space structures of 1D, 2D, and 3D crystals

Electron diffraction is one of the most powerful tools for investigating crystalline structures, particularly nanomaterials and material surfaces owing to their larger atomic scattering cross sections σ than those obtained with X-ray diffraction,

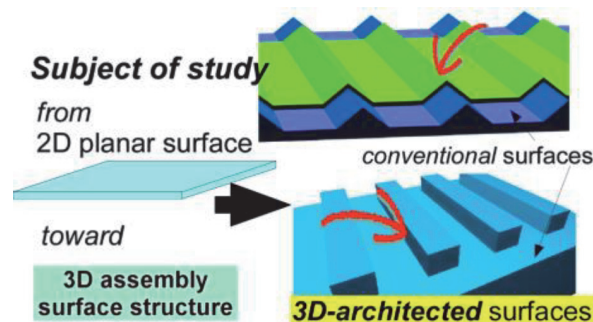


Figure 1.
Concept of our approach toward realizing atomically ordered 3D structures.

for instance, $\sigma \sim 4$ Mb for a 15 keV electron and 0.002 Mb for a Cu K (~ 8 keV) X-ray to a Si atom [10, 11]. According to the kinematic diffraction theory, a diffraction pattern can be understood as a reciprocal structure pattern reflecting a crystalline structure (Figure 2) in a reciprocal space map (RSM). By comparing an experimental reciprocal structure pattern in an RSM with patterns of candidate crystalline structures, we can analyze the characteristics of crystalline materials, such as dimensionality, atomic structure, orientation, size, and strain [4, 12–16].

For instance, an ideal one-dimensional (1D) material with lattice constant a in the x direction in real space (Figure 2(a)) shows a characteristic reciprocal structure pattern consisting of reciprocal lattice planes with a reciprocal lattice unit length of $a^* = 2\pi/a$ in the x direction (Figure 2(b)). This can be explained by the Bragg interference condition $a \cos \theta_{out} - a \cos \theta_{in} = n\lambda$, that is, $(\vec{k}_{out} - (\vec{k}_{in} + n\vec{a}^*)) \cdot \vec{e}_x = 0$. Here, λ is wavelength, and \vec{k}_{in} and \vec{k}_{out} are incident and outgoing wave-number vectors, respectively, satisfying $k_0 = |\vec{k}_{in}| = |\vec{k}_{out}| = 2\pi/\lambda$. Since the intersection of reciprocal lattice planes with an Ewald sphere of radius k_0 produces a diffraction pattern (Figure 2(c)), diffraction rings are observed as the diffraction patterns of 1D materials.

A 2D material with lattice constants a and b , that is, unit vectors \vec{a} and \vec{b} (Figure 2(d)), shows reciprocal lattice rods with reciprocal lattice unit vectors of \vec{a}^* and \vec{b}^* , corresponding to the intersection of orthogonal reciprocal lattice planes (Figure 2(e)). The intersection of reciprocal lattice rods with an Ewald sphere produces a pattern of diffraction spots arrayed on arcs. A reciprocal lattice rod at position $h\vec{a}^* + k\vec{b}^*$ is called an $(h\ k)$ rod, which produces an $(h\ k)$ 2D diffraction

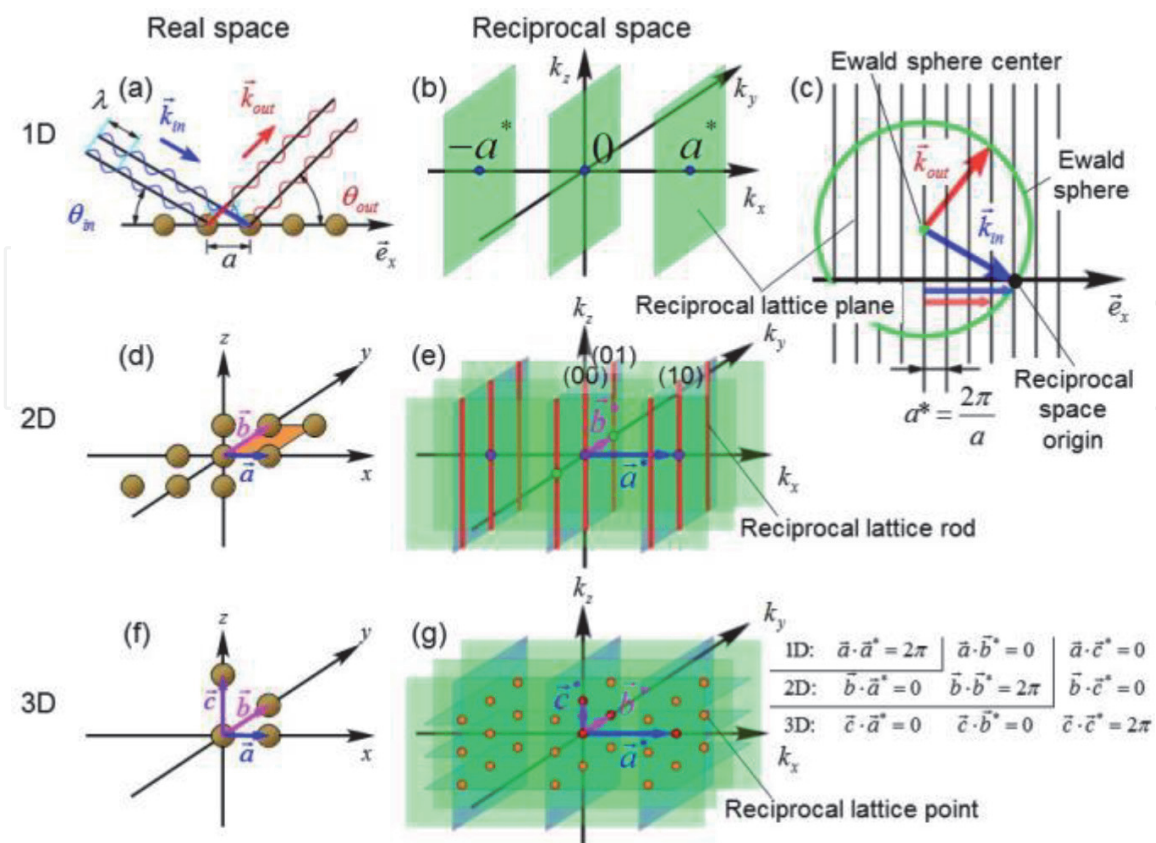


Figure 2. Schematics of (a)–(c) 1D, (d) and (e) 2D, and (f) and (g) 3D crystals: real space structures (a), (d), and (f) and corresponding reciprocal space structures (b), (c), (e), and (g). 1D, 2D, and 3D crystals show reciprocal lattice planes, reciprocal lattice rods, and reciprocal lattice points, respectively.

spot. A 3D material with unit vectors \vec{a} , \vec{b} , and \vec{c} (**Figure 2(f)**) shows reciprocal lattice points with unit vectors of \vec{a}^* , \vec{b}^* , and \vec{c}^* (**Figure 2(g)**). The intersection of reciprocal lattice points with an Ewald sphere produces a pattern of diffraction spots arrayed on a lattice. A reciprocal lattice point at position $h\vec{a}^*$, $k\vec{b}^*$, and $l\vec{c}^*$ produces an (hkl) 3D diffraction spot.

From diffraction patterns (e.g., diffraction rings or spots) projected on a detection screen, the original reciprocal structure pattern (e.g., reciprocal lattice planes, rods, or points) in a 3D RSM can be regenerated by changing the incident angle of the electron beam to the crystalline material (i.e., the direction of \vec{k}_{in}) or the beam energy (i.e., k_0), as illustrated in **Figure 3** for a 3D material with azimuth angle rotation [12–15]. For example, **Figure 4(a)** and **(b)** show a series of transmission electron diffraction patterns of a nanocrystal on a Si(001) substrate as a function of the azimuth angle around the substrate surface normal direction [14]. Indeed, the conversion of diffraction spots on a lattice (indicated by orange arrows) in different diffraction patterns generates reciprocal lattice points in a 3D RSM, as indicated by orange arrows in **Figure 4(c)–(e)**. In this 3D RSM, we can recognize the existence of a certain 3D crystalline structure, in this case the structure is α -FeSi₂, among candidate crystal structures [17, 18]; the crystalline orientations are α -FeSi₂(110) || Si(001) and α -FeSi₂[001] || Si<110> from the reciprocal structure pattern.

In **Figure 4(a)** and **(b)**, there are also diffraction spots on arcs indicated by red arrows. These spots are often observed under a glancing condition of an electron beam nearly parallel to a substrate surface in RHEED with a primary energy E_p of typically 10–15 keV. The conversion of the spots generates reciprocal lattice rods perpendicular to the substrate surface in a 3D RSM, as indicated by red arrows in **Figure 4(c)–(e)**. The existence of spots on arcs or reciprocal lattice rods implies that the surface perpendicular to the rods is atomically well-ordered; in this case, it implies the formation of a well-defined clean Si(001) substrate surface.

The width of a reciprocal lattice rod is finite (full width at half maximum $\simeq 2\pi/D$) and reflects the crystalline domain size D . Thus, the intersection of the rod with an Ewald sphere is elongated along the rod direction, that is, the surface normal direction. Indeed, in **Figures 4(a)** and **(b)** and **5(a)**, there are the surface spots (red arrows) elongated along the Si[001] substrate surface normal direction.

2.2 Diffraction patterns from side-surfaces of 3D structured sample

One of the advantages of RHEED is its ability to observe atomically ordered surfaces in any direction, as described later in Sections 3.2 and 4. RHEED has been used to investigate crystalline structures on planar substrate surfaces. Recently, for

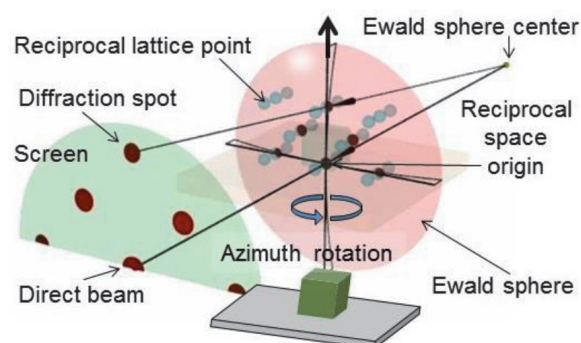


Figure 3. Schematic of relationship between diffraction spots and reciprocal lattice points intersecting with a partial Ewald sphere in 3D RSM, for 3D crystal.

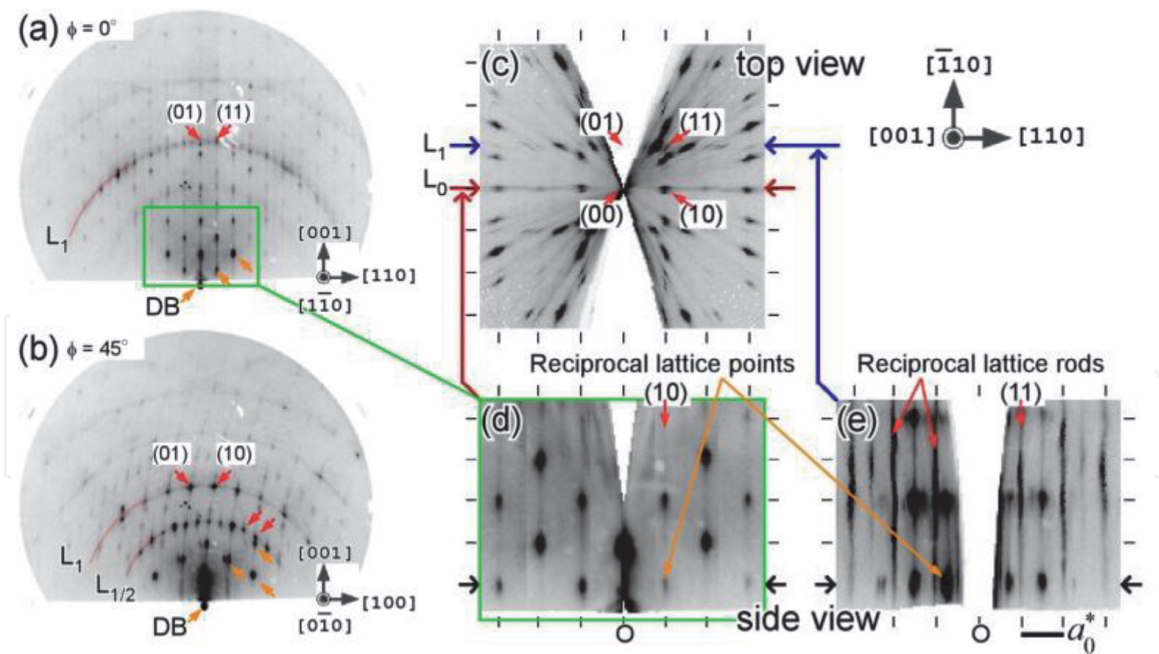


Figure 4. (a) and (b) RHEED patterns of $\alpha\text{-FeSi}_2(110)[001] \parallel \text{Si}(001)(110)$ at azimuth angles $\phi = 0^\circ$ and 45° , respectively. E_p is 15.0 keV ($k_o = 62.7 \text{ \AA}^{-1}$). (c) Top view and (d) and (e) side views of the 3D RSM regenerated from a series of RHEED patterns. In (a) and (b), diffraction spots indicated by orange and red arrows are assigned to reciprocal lattice points of 3D $\alpha\text{-FeSi}_2$ nanocrystals and reciprocal lattice rods of a 2D Si(001) substrate surface, respectively. Reciprocal lattice rods [e.g., (00) and (01)] lie on Laue zones (e.g., L_0 and L_1). DB denotes the direct beam position. $a_o^* = 2\pi/a_o \approx 2\pi/3.84 \text{ [\AA}^{-1}]$ is the reciprocal lattice unit length of $\text{Si}(001)1 \times 1$.

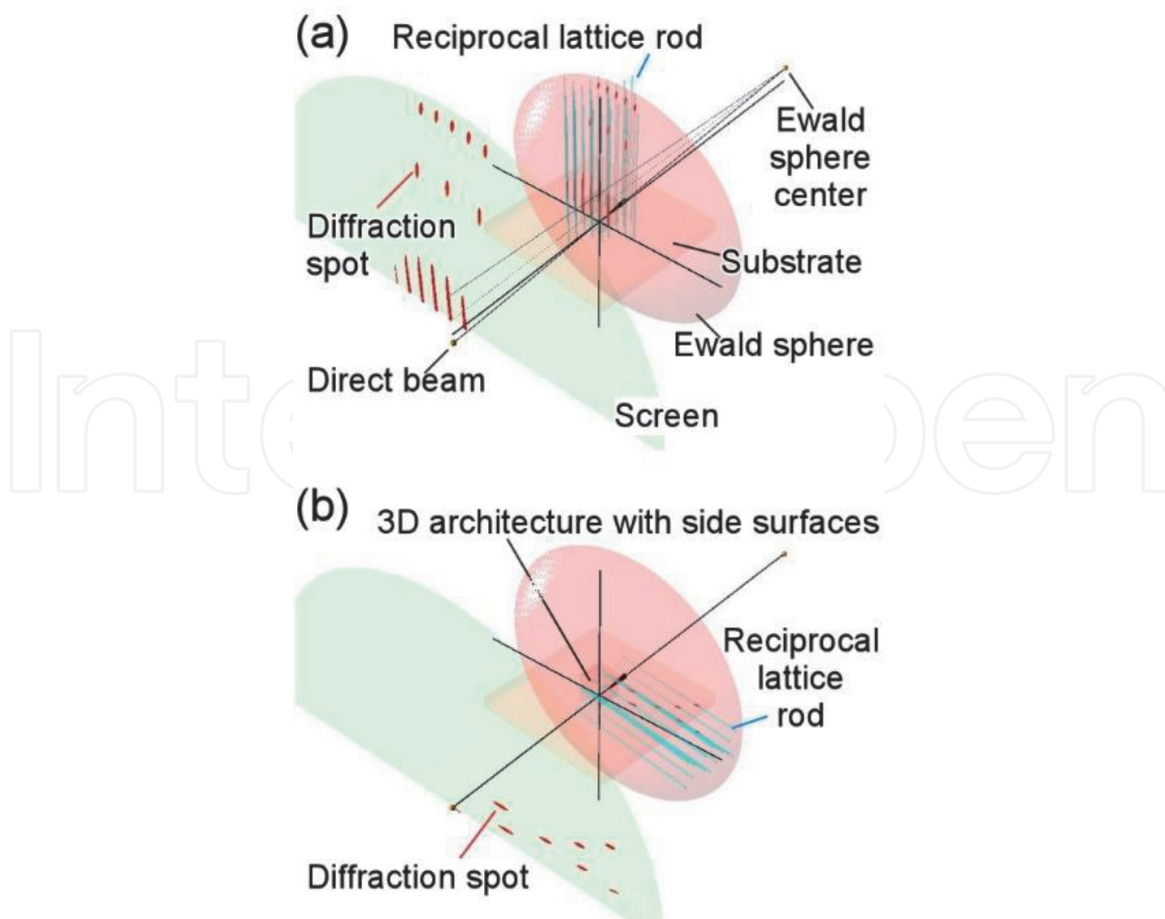


Figure 5. Schematics of 2D diffraction spots and reciprocal lattice rods of (a) substrate surface and (b) side-surface of 3D fabricated material. In both cases, diffraction spots are elongated in the surface normal direction.

3D fabricated materials, the authors have demonstrated that not only substrate surfaces but also surfaces inclined from or perpendicular to a substrate plane exhibit atomically ordered structures where surface spots elongated along directions inclined from or perpendicular to the substrate normal direction appear in RHEED patterns (**Figure 5(b)**) [6, 7, 9]. We emphasize that a simple surface property of 3D fabricated materials, that is, a surface direction, can be confirmed by the elongation of surface spots.

Low-energy electron diffraction (LEED) with a typical E_p of 50–100 eV focuses the interference caused by the backward scattering of an electron incident to an atom, while RHEED focuses the interference caused by forward scattering. Both LEED and RHEED are sensitive to surface structures. A LEED pattern at the normal incidence corresponds to a top view of reciprocal lattice rods intersecting with an Ewald sphere from the surface normal direction. The diffraction spots move to the (00) spot arising from the (00) rod with increasing E_p [8, 18]. For an inclined surface, the arrangement of diffraction spots in alignment changes that in an arc, the center of which is the (00) spot. The diffraction spots also move to the (00) spot with increasing E_p . Thus, we can confirm the surface direction of 3D fabricated materials by the arrangement and E_p -dependent motion of diffraction spots.

3. Experimental procedure

The authors demonstrated the creation of atomically ordered side- and facet-surfaces owing to the arbitrary selection of planes (**Figure 6**). Atomically reconstructed Si{100}, {110}, and {111} vertical side-surfaces and {111} tilted facet-surfaces were first realized on 3D patterned Si substrates, and the perfection of the 3D surface structures was examined. The {100}2×1, {110}16×2, and {111}7×7 diffraction spots from the 3D surfaces were confirmed by RHEED and LEED.

3.1 Sample fabrication with combination of dry and wet etching processes

The 3D architected Si samples with arbitrary faces discussed here were produced on commercial mirror-polished Si substrates by the following dry and wet etching procedures. All processes were performed at room temperature (RT). First, a line mask pattern was drawn using a photoresist. To produce the vertical side-surfaces (**Figure 7(a)–(c)**), Si was etched in an inductive coupled plasma (ICP)-reactive ion etching system (RIE-400iPB, Samco). The process parameters were an ICP source power of 300 W, a bias power of 10 W, and a working pressure of 4 Pa. Mixture gases of 10 sccm SF₆, 5 sccm O₂, and 200 sccm Ar were used in the etching cycle, and 40 sccm C₄F₈, 5 sccm O₂, and 200 sccm Ar were used in the passivation process [6–9]. Depending on dry RIE conditions, various curved structures from trapezoid to triangle shapes were obtained. When we produced tilted facet-surfaces (**Figure 7(d) and (e)**), the optimized conditions for a triangle-like shape were a

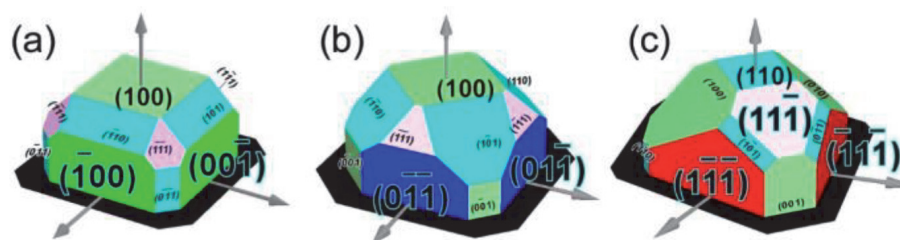


Figure 6.

(a)–(c) Schematic relationship among flat surface, vertical side-surfaces, and tilted facet-surfaces.

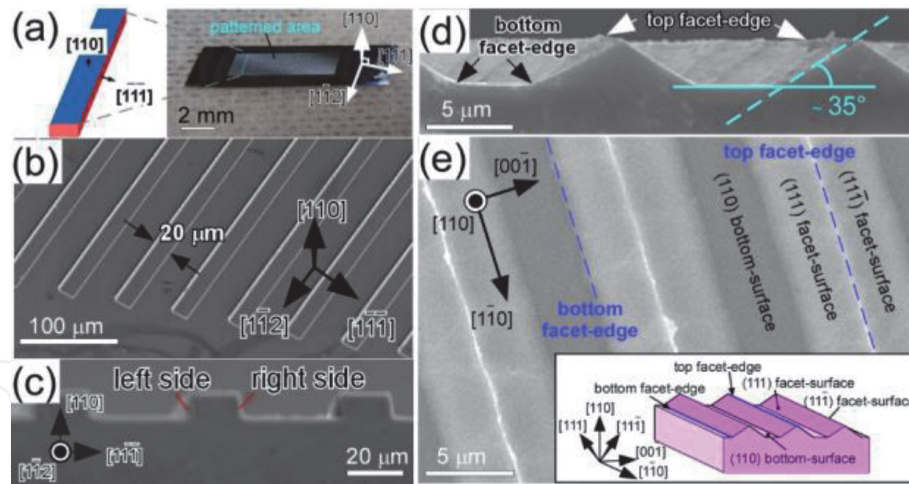


Figure 7.
 (a) Photograph of a 3D patterned Si(110) substrate consisting of {111} vertical side-surfaces. (b) Top and (c) cross-sectional SEM images of a patterned area. (d) Cross-sectional and (e) top SEM images of a sample with tilted {111} facet-surfaces.

flow rate of 51 sccm, a pressure of 4.0 Pa, and a bias power of 60 W using an RIE system (RIE-10 NR, Samco) with SF₆ gas [9].

After dry etching, wet etching was performed to reduce the side- and facet-surface roughnesses. The base solution used in the wet process removes the damage and contaminants [19–21], and flash annealing promotes reconstruction through the sublimation of the contaminants [22]. Unoptimized conditions never led to reconstructed patterns on side- or facet-surfaces. In this process, the etching recipe was optimized by considering the plane-dependent etching properties [23]. A {100} sample was dipped in 25 wt% tetramethylammonium hydroxide (TMAH) at 70°C for 3 min. A {110} sample was etched in 25 wt% TMAH with 0.1 vol% surfactant (iso-octylphenoxy polyethoxyethanol) at 70°C for 1 min [7]. Then, the sample was rinsed with pure water, dried by blowing with N₂, and introduced into an ultra-high vacuum (UHV) chamber. The 3D Si sample was degassed and flashed by direct-current heating at ~1150–1200°C at a pressure below 2×10^{-8} Pa.

3.2 RHEED observation of 3D structured samples

RHEED patterns were obtained at RT using an electron beam with an E_p of 15 keV and a diameter of ~0.5 mm. An advantage of the RHEED technique is the accessibility of various 3D surfaces; that is, the diffraction pattern consists of all diffractions from the substantial crystal surfaces in 3D space. Actually, the selection of the incident e-beam direction enables the identification of 3D surface structures. In this study, the direction of the incident electrons was defined by the glancing angle θ and azimuth angle ϕ for the top and bottom Si surfaces (Figure 8). The RHEED patterns were also obtained from the 3D samples with vertical side-surface or tilted facet-surfaces by controlling θ and ϕ . For instance, for 3D Si with a vertical {111} side-surface, θ is the angle between the incident electron beam and the top (110) surface, which was changed from -0.4° to $+1.2^\circ$. ϕ , which is defined as the angle from $[1\bar{1}2]$ in the in-plane direction, was changed from -4.5° to $+4.7^\circ$. The RHEED patterns were filtered by a computer to emphasize the spot features in the background. LEED can also be used to observe 3D surface ordering, while 3D accessibility is less than that of RHEED because of the limited range of diffraction conditions. LEED patterns were also observed using a typical E_p of 40–200 eV and a beam size of ~1 mm.

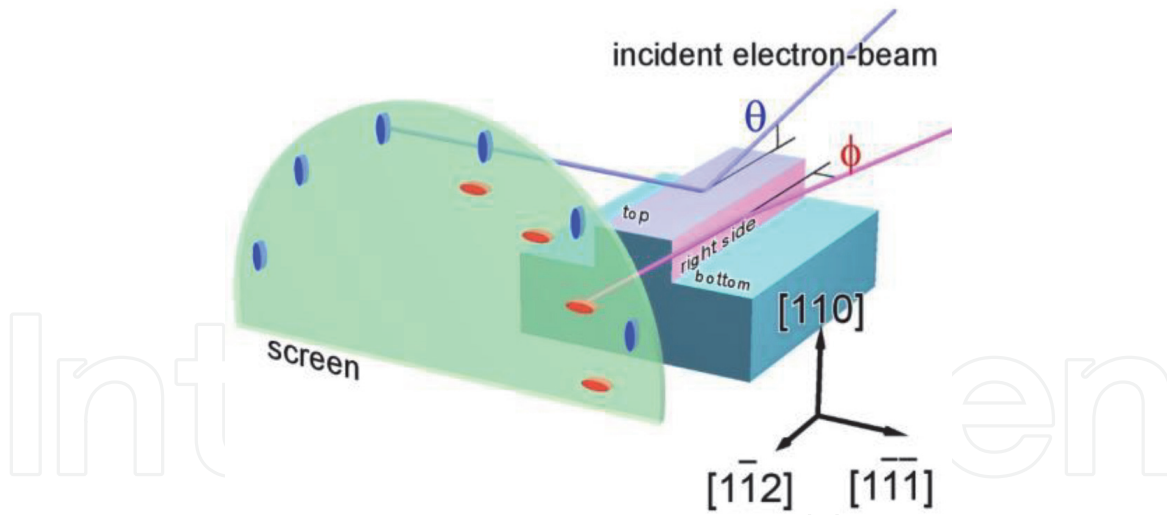


Figure 8. Schematic of the diffraction from the top- and side-surfaces of a 3D patterned Si(110) substrate. The control of the incident electron beam direction defined by θ and ϕ enables the observable faces in the 3D space to be selected.

4. Surface structures on 3D architected Si sample

4.1 {111} vertical side-surfaces

Figure 9(b)–(d) show typical filtered RHEED patterns obtained from 3D Si with a vertical {111} side-surface (**Figure 7(c)**) various θ and ϕ values. The {111} side-surfaces were produced on a (110) surface (**Figure 6(c)**). The RHEED patterns showed curious characteristics, because half of the patterns were removed, which has not been reported to the best of our knowledge. The appearance of the left-side

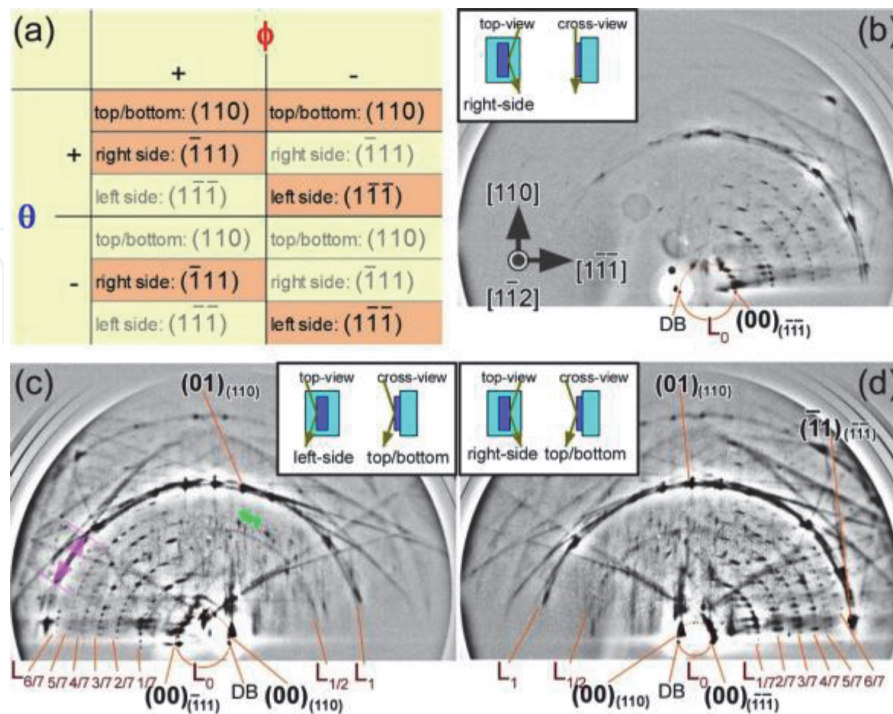


Figure 9. (a) Dependence of observable conditions (orange) in the RHEED pattern on the polarity of θ and ϕ . (b)–(d) RHEED patterns from 3D Si with {111} vertical side-surfaces observed at (b) $\theta = 0.0^\circ$ and $\phi = +1.9^\circ$, (c) $\theta = +0.3^\circ$ and $\phi = -1.6^\circ$, and (d) $\theta = +0.3^\circ$ and $\phi = +1.1^\circ$. Insets schematically show the relationship between the incident electron beam and the observable surfaces in 3D space.

and right-side $\text{Si}\{111\}7\times7$ patterns depends on ϕ , as shown in **Figure 9(c)** and **(d)**. ϕ is the azimuth angle for the $\text{Si}(110)$ top-/bottom-surfaces and simultaneously corresponds to the glancing angle for the $\text{Si}\{111\}$ side-surfaces. On the other hand, θ is the glancing angle for $\text{Si}(110)$ and is also the azimuth angle for $\text{Si}\{111\}$. **Figure 9(a)** summarizes the dependence of the observable and non-observable conditions in the RHEED patterns on the polarity of θ and ϕ . When θ (the glancing angle for $\text{Si}(110)$) decreases, the RHEED pattern from $\text{Si}(110)$ disappears, while a pattern from $\text{Si}\{111\}$ is present. Indeed, in **Figure 9(b)** ($\theta = 0.0^\circ$ and $\phi = +1.9^\circ$), a quarter circle 7×7 pattern with faint 2×16 spot can be seen. The diffraction spots on the left and the right sides (**Figure 7(c)**) are slightly elongated in the horizontal direction. In general, the elongation (streaky) direction corresponds to the surface normal direction [4], as illustrated in **Figure 8**. Thus, these slightly streaky spots indicate the existence of vertical side-surfaces.

Let us analyze the curious RHEED patterns in more detail. In **Figure 9(c)** ($\theta = +0.3^\circ$ and $\phi = -1.6^\circ$) and **Figure 9(d)** ($\theta = +0.3^\circ$ and $\phi = +1.1^\circ$), diffraction spots from the direct beam (DB) can be observed in the 1/7th-order Laue zones ($L_{1/7}$ - $L_{6/7}$) on the left and right quarter sides, respectively, as well as seven spots within the Kikuchi band width (e.g., indicated by a pink arrow in **Figure 9(c)**). These patterns clearly correspond to $\text{Si}\{111\}7\times7$ reconstruction [4], having shadow edges in the horizontal and vertical directions. **Figure 9(c)** (**Figure 9(d)**) corresponds to $\text{Si}(\bar{1}11)$ ($\text{Si}(1\bar{1}\bar{1})$) 7×7 diffraction on the surface of the left-side (right-side) wall of the 3D patterned structure. Note that a specular spot $(00)_{(\bar{1}11)}$ ($(00)_{(1\bar{1}\bar{1})}$) from the DB appears on the left (right) side. In addition, strong Kikuchi lines and bands were observed in the side RHEED pattern. These results indicate that atomically flat side-surfaces were achieved on 3D patterned $\text{Si}(110)$ by etching and UHV annealing.

One can see the characteristic ϕ and θ dependences of the RHEED patterns (movie) in Supporting Information of Ref [5]. These RHEED patterns clearly show that all the surfaces on 3D Si, that is, the (110) top-/bottom-surfaces, the $(1\bar{1}\bar{1})$ right-side surface, and the $(\bar{1}11)$ left-side surface, have atomically ordered structures.

Figure 10 shows the LEED patterns observed from the figured $(\bar{1}11)$ side-surface. Because in LEED we observe backscattering diffraction, while RHEED reflects forward scattering diffraction, a unique 3D Si sample with a wider side-surface was prepared [9]. A clear 7×7 pattern can be seen in **Figure 10(a)**, where the incident electron beam is along a direction almost normal to the $(\bar{1}11)$ side-surface. Characteristic LEED patterns were observed when the sample was rotated; the electron beam probed both a $(\bar{1}11)$ side-surface and a (110) top-surface. An example with an incident angle of $\sim 37^\circ$ is shown in **Figure 10(b)**, which reflects surface reconstructions for both the figured $(\bar{1}11)7\times7$ side-surface and the pristine $(110)16\times2$ top-surface [6].

The LEED patterns are in good agreement with those simulated by considering the crystal orientation and electron beam (i.e., the cross sections of the reciprocal lattice rods and an Ewald sphere [22]) shown in the lower-right panels of **Figure 10**. It is possible to identify diffraction spots on Laue zones of both $(\bar{1}11)$ and (110) surfaces in the patterns, demonstrating the observation of atomic crystalline ordering for the 3D surfaces using LEED.

4.2 $\{100\}$ vertical side-surfaces

Figure 11(a) shows a typical filtered RHEED pattern obtained from 3D Si with $\{100\}$ side-surfaces. The $\{100\}$ side-surfaces were created on a commercial mirror-polished $\text{Si}(100)$ substrate (**Figure 6(a)**). In **Figure 11(a)** ($\theta = +0.4^\circ$ and $\phi = -1.2^\circ$), the two overlapping $\text{Si}\{100\}2\times1$ reconstructed diffraction patterns [4, 24] originated

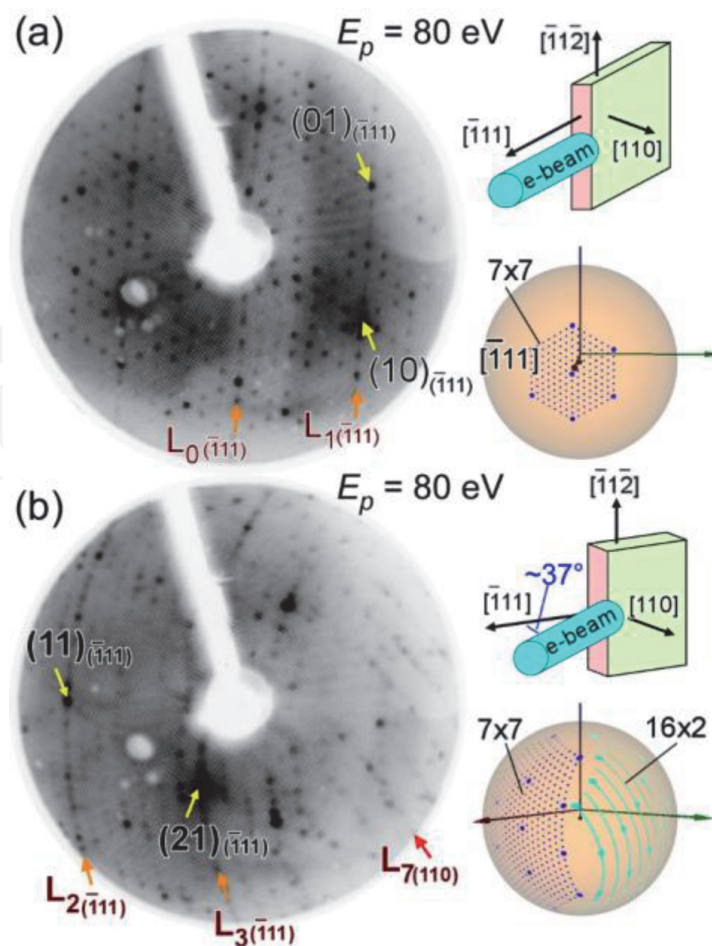


Figure 10.

LEED patterns for 3D Si sample with a wider $(\bar{1}\bar{1}1)$ side-surface at different incident angles of the electron beam with $E_p = 80$ eV: (a) normal incidence to the Si $(\bar{1}\bar{1}1)$ side-surface and (b) $\sim 37^\circ$ tilted from the normal direction. The relationship between the incident beam and the sample and the simulated LEED patterns are shown in the upper and lower right, respectively.

from the top/bottom and left-side surfaces. One is a (100) 2×1 pattern with a semicircular shape having a shadow edge $SE_{(100)}$ in the horizontal direction. The other is a (001) 2×1 pattern on the left quarter side with a shadow edge $SE_{(100)}$ in the vertical direction.

We can see that the diffraction spots on the left side are slightly elongated in the horizontal direction, which is a characteristic of a RHEED pattern from a side-surface [6]. The diffractions from the top-/bottom-surfaces disappeared and those from the left-side surface remained when we changed θ from $+0.4^\circ$ to 0.0° . When we set $\theta = +0.0^\circ$ and $\phi = -1.2^\circ$, only a quarter circle 2×1 pattern with strong Kikuchi lines and bands can be seen, corresponding to the relationship between θ and ϕ , that is, the glancing and azimuth angles for each surface, respectively, similarly to that observed in **Figure 9(a)**. Quarter circle 2×1 patterns were also observed on the right when ϕ was positive.

The left part of **Figure 11(b)** shows the reciprocal lattice of the Si $\{100\}2 \times 1$ reconstruction, corresponding to the left-side and top-/bottom-surfaces of the $\{100\}$ sample. The 2D reciprocal lattice of Si (001) is perpendicular to that of Si (100) with the common crystalline direction of $[0\bar{1}0]$. The Ewald constructions on the (100) top/bottom and (001) left-side surfaces in 3D reciprocal space in our experimental setup, namely, the simulated RHEED patterns at $\theta = +0.4^\circ$ and $\phi = -1.2^\circ$ (**Figure 11(b)** right panel), show good agreement with the observed RHEED pattern (**Figure 11(a)**). These results indicate that atomically flat side-surfaces were achieved on the $\{100\}$ sample.

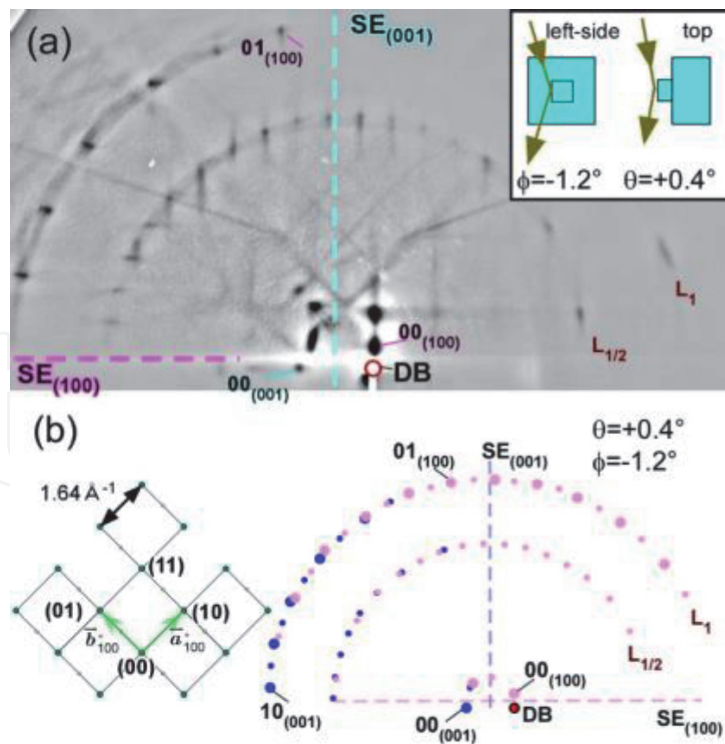


Figure 11. (a) RHEED pattern from the 3D Si sample with vertical $\{100\}$ side-surfaces at $\theta = +0.4^\circ$ and $\phi = -1.2^\circ$. The inset shows the relationship between the incident electron beam and the 3D surfaces. (b) Schematics of the 2D reciprocal lattices on $\{100\}2 \times 1$ reconstruction (left) and simulated RHEED pattern from the $\{100\}$ surfaces at $\theta = +0.4^\circ$ and $\phi = -1.2^\circ$.

4.3 $\{110\}$ vertical side-surfaces

Finally, the RHEED pattern from the vertical $\{110\}$ side-surface is shown in **Figure 12(a)**. Here, a $\{110\}$ side-surface was produced on a 2D(100) substrate (**Figure 6(b)**). **Figure 12(a)** shows the RHEED pattern from a $\{110\}$ sample at $\theta = +0.4^\circ$ and $\phi = +1.1^\circ$. A $\{110\}16 \times 2$ pattern can be seen in the right quarter, corresponding to the diffraction from the right-side $(0\bar{1}1)$ surface.

The weak spots in the arcs from the DB in the upper right, some of which are indicated by blue arcs, can be assigned to the Laue zone in the $(0\bar{1}1)$ plane ($L_0^{(0\bar{1}1)}$, $L_{1/16}^{(0\bar{1}1)}$, ..., $L_1^{(0\bar{1}1)}$) [24, 25] as shown in **Figure 12(c)**. The horizontal streaks from $L_{1/16}^{(0\bar{1}1)}$ to $L_1^{(0\bar{1}1)}$ represent the diffractions from (00) to (10) at the reciprocal lattice rods. Here, the reconstructed surface unit vectors from Si(110) 2×16 are defined as $\vec{a}_{s110}^* = 1/2\vec{a}_{110}^*$ and $\vec{b}_{s110}^* = 1/16\vec{a}_{110}^* + 1/16\vec{b}_{110}^*$ (domain A, purple points) and $\vec{a}_{s110}^* = 1/2\vec{a}_{110}^*$ and $\vec{b}_{s110}^* = -1/16\vec{a}_{110}^* + 1/16\vec{b}_{110}^*$ (domain B, green points), as shown in **Figure 12(a)**. In **Figure 12(a)**, domain A is only considered as a $(0\bar{1}1)$ eye guide. The incident electron direction was the [011] direction, and the first Laue zone arc of Si(100) of $L_1^{(100)}$ (**Figure 12(b)**) is the same as $L_1^{(0\bar{1}1)}$ (**Figure 12(d)**).

4.4 $\{111\}$ tilted facet-surfaces

Figure 13(a) shows a typical filtered RHEED pattern obtained from the $\{111\}$ facet sample at $\theta_g = +0.7^\circ$ and $\phi = +2.7^\circ$ after flashing in UHV. The RHEED pattern showed notable characteristics, consisting of tilted 7×7 spots (some are marked by yellow circles, and 1/7th-order Laue zones, $L_{1/7}$ - $L_{6/7}$, are recognized) and

faint horizontal 16×2 spots (cyan circles). The 7×7 pattern was tilted in the counterclockwise direction around DB, and the tilt angle was $\sim 36^\circ$, which is consistent with θ_F .

Figure 13(b) shows a simulated RHEED pattern from the (111) facet-surface, corresponding to Ewald sphere cross sections of 2D 7×7 reciprocal lattice rods of the tilted Si(111). The excellent agreement between **Figure 13(a)** and **(b)** indicates the creation of an atomically ordered Si(111) 7×7 facet-surface. The fabricated 3D structure shows that the relative glancing and azimuth angles to the tilted Si(111) facet-surface are 2.1 and 1.8° , respectively, under this condition. These RHEED patterns clearly show the existence of three different atomically ordered surfaces on the $\{111\}$ facet sample, that is, the (110) bottom, (111) facet, and $(\bar{1}\bar{1}\bar{1})$ facet-surfaces. One can see the characteristic ϕ dependence of the RHEED patterns in Ref [9].

5. Application of 3D architected Si

The creation and observation methods for well-defined surfaces enable the epitaxial growth of an arbitrary geometry, a key technique for nanoconstruction in 3D space [26–31]. Therefore, our established methodology contributes to the realization of well-ordered 3D nanofabrication, where the material stacking direction can be perfectly switched between the out-of-plane and in-plane directions. Novel 3D nanostructures are also expected to help unveil the underlying 3D surface science phenomena. Finally, two demonstrations utilizing a 3D architected Si platform are shown.

5.1 Platform for material growth on 3D surfaces

Atomically well-defined side-surfaces on a substrate can make an enormous contribution to nanofabrication [26–31]. To demonstrate the applicability of material growth on such side-surfaces, we produced Si $\{111\}$ -Fe and Si $\{111\}$ -Ag reconstructed side-surface structures on 3D Si with vertical $\{111\}7 \times 7$ side-surfaces. Ag and Fe layers with thickness of 1.0 and 0.4 nm were deposited on the $(\bar{1}\bar{1}\bar{1})$ left-side and $(\bar{1}\bar{1}\bar{1})$ right-side surfaces, respectively, and the sample was subsequently annealed at 500°C in UHV.

Figure 14(a) and **(b)** show typical RHEED patterns obtained from the left-side and right-side surfaces, respectively. We can confirm $\sqrt{3} \times \sqrt{3}$ (streaky) spots in L_0 (orange arrows) in **Figure 14(a)**. In **Figure 14(b)**, we can confirm 2×2 (streaky) spots (orange arrows), showing the formation of c-FeSi [18]. Simultaneously, Si $(\bar{1}\bar{1}\bar{1})\sqrt{3} \times \sqrt{3}$ -Ag [4, 24, 31, 32] was obtained on the left-side surface. These results show that highly developed thin-film formation techniques are applicable for the vertical side-surface of 3D patterned substrates and the material stacking direction can be perfectly switched between the out-of-plane and in-plane directions.

Figure 14(c) and **(d)** show cross-sectional TEM images of the 0.4-nm-thick Fe layer deposited on the $(\bar{1}\bar{1}\bar{1})$ right-side surface and the 5.0-nm-thick Ag deposited on the $(\bar{1}\bar{1}\bar{1})$ left-side surface. We can see four and five MLs of α -Fe [18] on the $(\bar{1}\bar{1}\bar{1})$ right-side surface (**Figure 14(d)**), where a smooth in-plane heteroepitaxial interface with a length of 50 nm or more was formed between α -Fe and Si. The orientation relations between the α -Fe and the Si right-side surface are $(\bar{1}\bar{1}\bar{1})_{\text{Fe}} \parallel (\bar{1}\bar{1}\bar{1})_{\text{Si}}$ and $[\bar{1}\bar{1}\bar{2}]_{\text{Fe}} \parallel [\bar{1}\bar{1}\bar{2}]_{\text{Si}}$, similar to those indicated in previous reports on Fe on a 2D Si(111) surface [18, 33, 34]. A cross-sectional TEM image for Ag deposited on the $(\bar{1}\bar{1}\bar{1})$

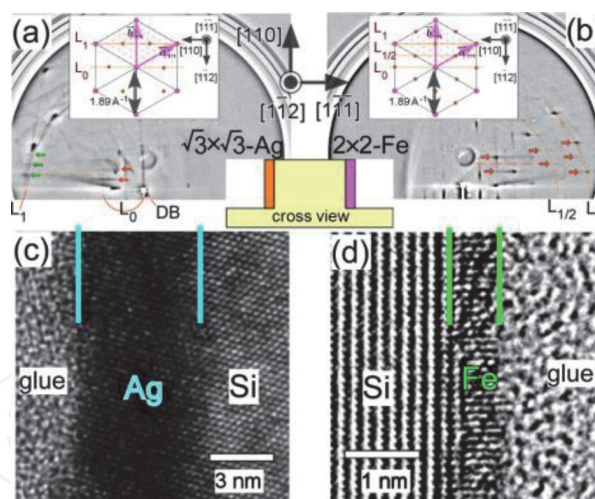


Figure 14.

RHEED patterns obtained from (a) $\text{Si}(\bar{1}\bar{1}\bar{1})$ -Ag left-side surface and (b) $\text{Si}(1\bar{1}\bar{1})$ -Fe right-side surface annealed at 773 K in UHV. Spots in the L_0 Laue zone indicated by orange arrows correspond to the $\sqrt{3} \times \sqrt{3}$ reciprocal lattice rods in (a), and spots indicated by orange arrows correspond to the 2×2 superstructure in (b). Cross-sectional TEM images of (c) Ag-deposited and (d) Fe-deposited side-surfaces at RT.

left-side surface (**Figure 14(c)**) showed that fcc-Ag epitaxially grew with an atomically matched interface, $\text{Ag}(\bar{1}\bar{1}\bar{1}) \parallel \text{Si}(\bar{1}\bar{1}\bar{1})$, without any visible defects or dislocations.

Our results clearly show that a coherently grown (ultra) thin film was realized on the vertical side-surface with the growth alternating between the out-of-plane and in-plane directions. The siliciding reaction can be controlled on the side-surfaces. Therefore, highly developed thin-film formation techniques are applicable for the vertical side-surface of 3D patterned substrates, and the material stacking direction can be perfectly switched between the out-of-plane and in-plane directions.

5.2 Novel conductivity on interconnected $\{100\}$ vertical side-surfaces

Three-dimensional integrated circuits, which contain multiple layers of active devices, have the potential to dramatically enhance chip performance, functionality, and device packing density. Recent 3D structured field-effect transistors (FETs) have surfaces with different orientations; for instance, a fin-type tri-gate structure has one top-surface and two side-surfaces [35, 36].

The electric connection between metal wires on these surfaces—that is, the wiring interconnects at sharp edges of top- and side-surfaces—is one of the issues in the development of 3D devices. Although the conductivity in metal wires on isolated 2D planar or side-surfaces has been well discussed, there are no reports on the metal conductivity of interconnections between 3D surfaces with different orientations, probably owing to the difficulty in measuring the intrinsic conductivity in 3D angular interconnects, which is mainly caused by diffuse scattering on rough surfaces [37–48]. One of the most outstanding factors contributing to the conductivity in the 3D angular interconnects is the facet-edge, which is a boundary of two surfaces with different crystalline orientations. To extract an intrinsic conductive property for metal wires interconnected at facet-edges, atomically flat surfaces in 3D structured substrates are required for the evaluation of the 3D interconnect resistivity by eliminating extra factors, such as roughness. To elucidate the impact of the 3D geometric effect on the conductive property, angularly interconnected Au wires with two configurations, crossing over and parallel to the facet-edges, were produced on atomically flat facet $\{111\}$ surfaces (**Figure 13**).

Figure 15(a) shows a typical cross-sectional SEM image of a $\{111\}$ facet sample on which a 10-nm-thick Au layer was deposited. The SEM image indicates that Au

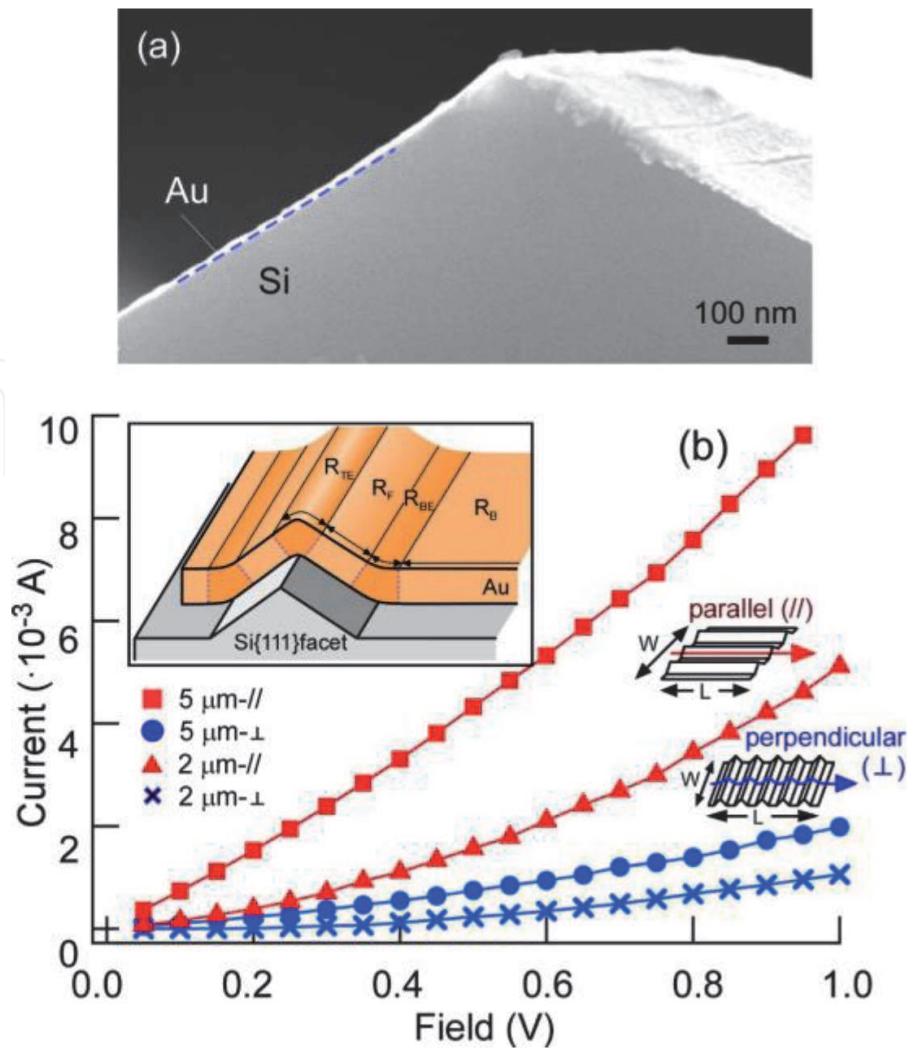


Figure 15. (a) Typical SEM image for a facet sample on which a 10-nm-thick Au layer was deposited. (b) Current vs. voltage curves of Au wires with the channel area ($W \times L$) of 2×100 and $5 \times 100 \mu\text{m}^2$ at 100 K in the parallel (red) and perpendicular (blue) configurations (insets). The upper left inset shows a schematic of the Au film on the Si{111} facet sample. The Au film is assumed to consist of bottom-surface (B), facet-surface (F), top facet-edge (TE), and bottom facet-edge (BE) regions with resistivity of R_B , R_F , R_{TE} , and R_{BE} , respectively.

was uniformly grown on the Si facet-surface with a smooth interface without any depressions or protrusions. No breaks or discontinuity of the Au wires was observed in SEM images, even at the top facet-edges. **Figure 15(b)** shows current-voltage properties at 100 K for 3D angularly interconnected Au wires of 2 μm width (circles) and 5 μm width (squares) in the parallel (red) and perpendicular (blue) configurations (insets). The length of the Au wires was 100 μm . Both perpendicular wires have an approximately one-order larger resistance (smaller current) than the parallel wires of the same width. For the other wire widths, the resistance in the perpendicular configuration was also larger than that in the parallel configuration.

The simplified resistance ratio, defined as the inverse of the current ratio at a fixed voltage, was 3–10 for the measured wire widths. Note that the dimensions (cross section and length) and crystallinity of the Au film were almost the same in the parallel and perpendicular configurations. Thus, the significant anisotropic resistance in these configurations is ascribed to the properties of the geometric shapes of the Au wires, that is, 3D angular interconnects. Indeed, the perpendicular wires have more facet-edges than the parallel wires; the perpendicular channel crossed over 11 top and 23 bottom facet-edges, while the parallel channel crossed over one top and two bottom facet-edges for a wire width of 5 μm .

Au wires on the 3D facet structure can be separated into four regions: flat bottom-surface, flat facet-surface, convex top facet-edge, and concave bottom facet-edge regions with resistances of R_B , R_F , R_{TE} , and R_{BE} , respectively, as shown in the inset of **Figure 15(b)**. The geometries of crystal grain boundaries in the polycrystalline Au wire may increase the electrical resistance [49]. The aggregation of crystal grain boundaries in the interconnect region, leading to the reduction in effective cross-sectional area, was attributed to the large α (≈ 30 – 180), i.e.,

$$R_B = R_F \sim \alpha R_{TE}, \sim \alpha R_{BE}.$$

We found that the conductivity passing through the interconnects is sensitive to the alignment of the facet-edges in the electric path, and the series configuration showed a 3–10-fold larger resistance than the parallel configuration, which originated from the increased resistivity across the facet-edges by a factor of ~ 30 – 180 , as calculated from the circuit model. This work provides a fundamental understanding of the impact of the 3D angular interconnects of a metal wire on electric transport and guidelines for the comprehensive investigation of the intrinsic interconnect transport properties on 3D structures, which is expected to produce critical benefits in the semiconductor industry.

6. Conclusion

This chapter demonstrated the creation and evaluation of atomically ordered side-surfaces and inclined facet-surfaces in nanofabricated 3D Si architectures toward the realization of sequentially 3D integrated and stacked devices for More Moore [3]. Atomically flat and well-ordered 3D structured surfaces play an important role in creating high-performance films on arbitrarily oriented 3D surfaces, similar to films grown on ordinary planar substrates. We emphasized that electron diffraction techniques such as RHEED and LEED are convenient for evaluating atomically ordered 3D surfaces, while conventional SEM has no atomic resolution. The points for recognizing 3D surfaces in diffraction patterns were explained along the basic concept of diffraction in reciprocal space; the intersection of reciprocal lattice rods with an Ewald sphere led to diffraction spots on arcs, and the spots elongate in the surface normal direction.

By diffraction, we evaluated several systems with side- or facet-surfaces of Si $\{111\}$ or $\{100\}$ on Si(110) or Si(001) substrates, which were fabricated by lithography dry and wet etching processes, followed by annealing in vacuum. Metal deposition on the well-ordered 3D surfaces (followed by annealing) also produced well-ordered films of nanometer thickness fabricating with arbitrary orientations. This is one of the fundamental techniques for defect-free material construction on 3D architectures. The electrical conductivity of metal wires on atomically flat 3D facet-surfaces crossing facet-edges was also measured toward the design of nano-scale steric wiring. We consider that these techniques for creating and evaluating 3D surfaces are promising for the realization of future 3D architecture devices.

Acknowledgements

The authors appreciate Dr. Shohei Takemoto, Dr. Haoyu Yang, Prof. Hiroshi Daimon, and Prof. Hidekazu Tanaka for their contribution to these studies. We also thank Ms. Saeko Tonda, Ms. Michiko Sakuma, Mr. Shoichi Sakakihara, and Mr. Takeshi Ishibashi for their helpful support in the fabrication of 3D Si samples and Ms. Liliany N. Pamasi and Mr. Ken Maetani for their support in the diffraction measurement of Si samples. This work was partially supported by Adaptable and

Seamless Technology Transfer Program through target-driven R&D (A-STEP) from the Japan Science and Technology Agency (JST) (No. JPMJTM19CM), Japan Society for the Promotion of Science (JSPS) Grant-in-Aid for Scientific Research B (Nos. 18H01871 and 20H02483), the Nanotechnology Platform Project (Nanotechnology Open Facilities in Osaka University, Nos. F-16-OS-0012 and F-16-OS-0016), and the Research Program of “Dynamic Alliance for Open Innovation Bridging Human, Environment and Materials” in “Network Joint Research Center for Materials and Devices” (No. 20203017).

IntechOpen

Author details

Azusa N. Hattori¹ and Ken Hattori^{2*}

¹ Institute of Scientific and Industrial Research, Osaka University, Ibaraki, Osaka, Japan

² Graduate School of Science and Technology, Nara Institute of Science and Technology, Ikoma, Nara, Japan

*Address all correspondence to: khattori@ms.naist.jp

IntechOpen

© 2020 The Author(s). Licensee IntechOpen. This chapter is distributed under the terms of the Creative Commons Attribution License (<http://creativecommons.org/licenses/by/3.0>), which permits unrestricted use, distribution, and reproduction in any medium, provided the original work is properly cited. 

References

- [1] Moore GE. Cramming more components onto integrated circuits. *Electronics*. 1969;**38**:114. DOI: 10.1109/N-SSC.2006.4785860
- [2] Zheng H, Wang J, Lofland SE, Ma Z, Mohaddes-Ardabili L, Zhao T, et al. Multiferroic BaTiO₃-CoFe₂O₄ nanostructures. *Science*. 2004;**303**:661. DOI: 10.1126/science.1094207
- [3] International Roadmap for Devices and Systems. Available from: <https://irds.ieee.org/>
- [4] Ichimiya A, Cohen PI. *Reflection High-Energy Electron Diffraction*. Cambridge: Cambridge University Press; 2004. DOI: 10.1017/CBO9780511735097
- [5] Van Hove MA, Weinberg WH, Chan C-M. Low-energy electron diffraction: Experiment, theory and surface structure determination. In: *Springer Series in Surface Sciences 6*. Berlin: Springer; 1986. DOI: 10.1007/978-3-642-82721-1
- [6] Hattori AN, Hattori K, Takemoto S, Daimon H, Tanaka H. Creation of atomically flat Si{111}7×7 side-surfaces on a three-dimensionally-architected Si(110) substrate. *Surface Science*. 2016; **644**:86. DOI: 10.1016/j.susc.2015.09.002
- [7] Hattori AN, Takemoto S, Hattori K, Daimon H, Tanaka H. Methods of creating and observing atomically reconstructed vertical Si{100}, {110}, and {111} side surfaces. *Applied Physics Express*. 2016;**9**:085501. DOI: 10.7567/APEX.9.085501
- [8] Yang H, Hattori AN, Ohata A, Takemoto S, Hattori K, Daimon H, et al. Direct observation for atomically flat and ordered vertical 111 side-surfaces on three-dimensionally figured Si(110) substrate using scanning tunneling microscopy. *Japanese Journal of Applied Physics*. 2017;**56**:111301. DOI: 10.7567/jjap.56.111301
- [9] Takemoto S, Hattori AN, Hattori K, Tanaka H, Daimon H. Electric transport properties for three-dimensional angular-interconnects of Au wires crossing facet edges of atomically-flat Si{111} surfaces. *Japanese Journal of Applied Physics*. 2018;**57**:085503. DOI: 10.7567/JJAP.57.090303
- [10] Tanuma S, Powell CJ, Penn DR. Calculations of electron inelastic mean free paths (IMFPs). IV. Evaluation of calculated IMFPs and of the predictive IMFP formula TPP-2 for electron energies between 50 and 2000 eV. *Surface and Interface Analysis*. 1993;**20**: 77. DOI: 10.1002/sia.740200112
- [11] Thompson AC, Attwood DT, Gullikson EM, Howells MR, Kim K-J, Kirz J, et al. *X-Ray Data Booklet*. California: Center for X-ray Optics and Advanced Light Source, Lawrence Berkeley National Laboratory; 2001. Available from: <https://xdb.lbl.gov/>
- [12] Romanyuk O, Kataoka K, Matsui F, Hattori K, Daimon H. Structure analysis of thin iron-silicide film from ϕ -scan RHEED Patterson function. *Czechoslovak Journal of Physics*. 2006; **56**:267. DOI: 10.1007/s10582-006-0087-5
- [13] Abukawa T, Yamazakai T, Yajima K, Yoshimura K. Weissenberg reflection high-energy electron diffraction for surface crystallography. *Physical Review Letters*. 2006;**97**: 245502. DOI: 10.1103/PhysRevLett.97.245502
- [14] Someta M, Maetani K, Hattori K, Daimon H. Phase discrimination of iron-silicides on Si(001) surfaces by three-dimensional reciprocal-lattice mapping. *Surface Science*. 2010;**604**:21. DOI: 10.1016/j.susc.2009.10.010

- [15] Hattori H, Oi H, Tanaka K, Kumagai T, Daimon H. Three-dimensional reciprocal-lattice analysis using azimuth-scan reflection high-energy electron diffraction: Determination of complex crystal orientations of Al grains on Si(111) surface. *Japanese Journal of Applied Physics*. 2012;**51**:055801. DOI: 10.1143/JJAP.51.055801
- [16] Takemoto S, Hattori K, Someta M, Hattori AN, Tanaka H, Kurushima K, et al. Shape-fitting analyses of two-dimensional X-ray diffraction spots for strain-distribution evaluation in a β -FeSi₂ nano film. *Journal of Applied Crystallography*. 2019;**52**:732. DOI: 10.1107/S1600576719007234
- [17] Nakano H, Maetani K, Hattori K, Daimon H. Variety of iron silicides grown on Si(001) surfaces by solid phase epitaxy: Schematic phase diagram. *Surface Science*. 2007;**601**: 5088. DOI: 10.1016/j.susc.2007.04.234
- [18] Kataoka K, Hattori K, Miyatake Y, Daimon H. Iron silicides grown by solid phase epitaxy on a Si(111) surface: Schematic phase diagram. *Physical Review B*. 2006;**74**:155406. DOI: 10.1103/PhysRevB.74.155406
- [19] Liang E-Z, Huang C-J, Lin C-F. Use of SiO₂ nanoparticles as etch mask to generate Si nanorods by reactive ion etch. *Journal of Vacuum Science and Technology B*. 2006;**24**:599. DOI: 10.1116/1.2172251
- [20] Ng AMC, Dong L, Ho WK, Djurišić AB, Xie MH, Wu HS, et al. Recovery of clean ordered (111) surface of etched silicon. *Applied Surface Science*. 2013;**282**:156. DOI: 10.1016/j.apsusc.2013.05.092
- [21] Wu B, Kumar A, Pamarthy S. High aspect ratio silicon etch: A review. *Journal of Applied Physics*. 2010;**108**: 051101. DOI: 10.1063/1.3474652
- [22] Oura K, Lifshits VG, Saranin A, Zotov AV, Katayama M. *Surface Science: An Introduction (Advanced Texts in Physics)*. Berlin: Springer; 2003. DOI: 10.1007/978-3-662-05179-5
- [23] Pal P, Gosalvez MA, Sato K. Silicon micromachining based on surfactant-added tetramethyl ammonium hydroxide: Etching mechanism and advanced applications. *Japanese Journal of Applied Physics*. 2010;**49**:056702. DOI: 10.1143/JJAP.49.056702
- [24] Lifshits VG, Saranin AA, Zotov AV. *Surface Phases on Silicon: Preparation, Structures, and Properties*. Chichester: Wiley; 1994. ISBN 0-471-94846-2
- [25] Yamamoto Y, Ino S, Ichikawa T. Surface reconstruction on a clean Si(110) surface observed by RHEED. *Japanese Journal of Applied Physics*. 1986;**25**:L331. DOI: 10.1143/JJAP.25.L331
- [26] Hattori AN, Fujiwara Y, Fujiwara K, Murakami Y, Shindo D, Tanaka H. Fabrication of three-dimensional epitaxial (Fe,Zn)₃O₄ nanowall wire-structures and their transport properties. *Applied Physics Express*. 2014;**7**:045201. DOI: 10.7567/APEX.7.045201
- [27] Fujiwara Y, Hattori AN, Fujiwara K, Tanaka H. Nanowall shaped MgO substrate with flat (100) sidesurface: A new route to three-dimensional functional oxide nanostructured electronics. *Japanese Journal of Applied Physics*. 2012;**52**:015001. DOI: 10.7567/JJAP.52.015001
- [28] Hattori AN, Fujiwara Y, Fujiwara K, Tanaka H. 3D-architected and integrated metal oxides nanostructures and beyond by three-dimensional nanotemplate pulsed-laser deposition. *e-Journal of Surface Science and Nanotechnology*. 2015;**13**:279. DOI: 10.1380/ejssnt.2015.279
- [29] Hattori AN, Fujiwara Y, Fujiwara K, Nguyen TVA, Nakamura T, Ichimiya M,

- et al. Identification of Giant Mott phase transition of single electric nanodomain in manganite nanowall wire. *Nano Letters*. 2015;**15**:4322. DOI: 10.1021/acs.nanolett.5b00264
- [30] Tsubota S, Hattori AN, Nakamura T, Azuma Y, Majima Y, Tanaka H. Enhancement of discrete changes in resistance in engineered VO₂ heterointerface nanowall wire. *Applied Physics Express*. 2017;**10**:115001. DOI: 10.7567/JJAP.57.090303
- [31] Rakshit R, Hattori AN, Naitoh Y, Shima H, Akinaga H, Tanaka H. Three-dimensional nanoconfinement supports Verwey transition in Fe₃O₄ nanowire at 10 nm length scale. *Nano Letters*. 2019; **19**:5003. DOI: 10.1021/acs.nanolett.9b01222
- [32] Le Lay G. Physics and electronics of the noble-metal/elemental-semiconductor interface formation: A status report. *Surface Science*. 1983;**132**: 169. DOI: 10.1016/B978-0-444-86784-1.50019-5
- [33] Shimizu S, Sasaki N, Seki S. Epitaxial growth of α -Fe film on Si(111) substrate by low-energy direct ion beam deposition. *Japanese Journal of Applied Physics*. 1993;**32**:L943. DOI: 10.1143/JJAP.32.L943
- [34] Shimizu S, Sasaki N. Crystalline quality of α -Fe films on Si(111) and Ge(111) substrates grown by direct ion beam deposition. *Thin Solid Films*. 1996; **281-282**:46. DOI: 10.1016/0040-6090(96)08572-0
- [35] Hisamoto D, Lee W-C, Kedzierski J, Takeuchi H, Asano K, Kuo C, et al. FinFET-a self-aligned double-gate MOSFET scalable to 20 nm. *IEEE Transactions on Electron Devices*. 2000; **47**:2320. DOI: 10.1109/16.887014
- [36] Colinge J-P. Multiple-gate SOI MOSFETs. *Solid State Electronics*. 2004; **48**:897. DOI: 10.1016/j.sse.2003.12.020
- [37] Krastev ET, Voice LD, Tobin RG. Surface morphology and electric conductivity of epitaxial Cu(100) films grown on H-terminated Si(100). *Journal of Applied Physics*. 1996;**79**:6865. DOI: 10.1063/1.361508
- [38] Luo EZ, Heun S, Kennedy M, Wollschläger J, Henzler M. Surface roughness and conductivity of thin Ag films. *Physical Review B*. 1994;**49**:4858. DOI: 10.1103/PhysRevB.49.4858
- [39] Chawla JS, Gstrein F, O'Brien KP, Clarke JS, Gall D. Electron scattering at surfaces and grain boundaries in Cu thin films and wires. *Physical Review B*. 2011;**84**:235423. DOI: 10.1103/PhysRevB.84.235423
- [40] Mao K, Saraya T, Hiramoto T. Effects of side surface roughness on carrier mobility in tri-gate single silicon nanowire metal-oxide-semiconductor field-effect transistors. *Japanese Journal of Applied Physics*. 2013;**52**:04CC11. DOI: 10.7567/JJAP.52.04CC11
- [41] Elsom KC, Sambles JR. Macroscopic surface roughness and the resistivity of thin metal films. *Journal of Physics F: Metal Physics*. 1981;**11**:647. DOI: 10.1088/0305-4608/11/3/012
- [42] Lee SC, Neumann A, Jiang Y-B, Artyushkova K, Brueck SRJ. Top-down, in-plane GaAs nanowire MOSFETs on an Al₂O₃ buffer with a trigate oxide from focused ion-beam milling and chemical oxidation. *Nanotechnology*. 2016;**27**:375707. DOI: 10.1088/0957-4484/27/37/375707
- [43] Goodnick SM, Ferry DK, Wilmsen XW, Liliental Z, Fathy D, Krivanek OL. Surface roughness at the Si(100)-SiO₂ interface. *Physical Review B*. 1985;**32**:8171. DOI: 10.1103/PhysRevB.32.8171
- [44] Mou C-Y, Hong T-M. Transport in quantum wells in the presence of interface roughness. *Physical Review B*.

2000;**61**:12612. DOI: 10.1103/
PhysRevB.61.12612

[45] Wang J, Polizzi E, Ghosh A, Datta S, Lundstrom M. Theoretical investigation of surface roughness scattering in silicon nanowire transistors. *Applied Physics Letters*. 2005;**87**:043101. DOI: 10.1063/1.2001158

[46] Buran C, Pala MG, Bescond M, Dubois M, Mouis M. Three-dimensional real-space simulation of surface roughness in silicon nanowire FETs. *IEEE Transactions on Electron Devices*. 2009;**56**:2186. DOI: 10.1109/TED.2009.2028382

[47] Kim SG, Luisier M, Paul A, Boykin TB, Klimeck G. Full three-dimensional quantum transport simulation of atomistic Interface roughness in silicon nanowire FETs. *IEEE Transactions on Electron Devices*. 2011;**58**:1371. DOI: 10.1109/TED.2011.2118213

[48] Ryu H. A multi-subband Monte Carlo study on dominance of scattering mechanisms over carrier transport in sub-10-nm Si nanowire FETs. *Nanoscale Research Letters*. 2016;**11**:36. DOI: 10.1186/s11671-016-1249-4

[49] Lee H-Y, Yi S-M, Lee J-H, Lee H-S, Hyun S, Joo Y-C. Effects of bending fatigue on the electrical resistance in metallic films on flexible substrates. *Metals and Materials International*. 2010;**16**:947. DOI: 10.1007/s12540-010-1213-2